

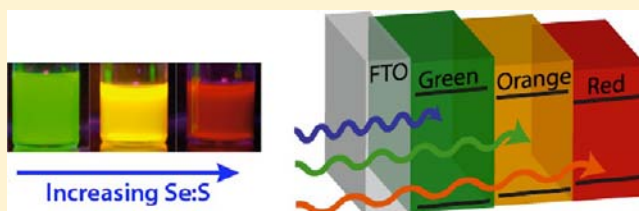
Tandem-Layered Quantum Dot Solar Cells: Tuning the Photovoltaic Response with Luminescent Ternary Cadmium Chalcogenides

Pralay K. Santra and Prashant V. Kamat*

Radiation Laboratory, Department of Chemistry and Biochemistry and Department of Chemical and Biomolecular Engineering, University of Notre Dame, Notre Dame, Indiana 46556, United States

S Supporting Information

ABSTRACT: Photon management in solar cells is an important criterion as it enables the capture of incident visible and infrared photons in an efficient way. Highly luminescent CdSeS quantum dots (QDs) with a diameter of 4.5 nm were prepared with a gradient structure that allows tuning of absorption and emission bands over the entire visible region without varying the particle size. These crystalline ternary cadmium chalcogenides were deposited within a mesoscopic TiO₂ film by electrophoretic deposition with a sequentially-layered architecture. This approach enabled us to design tandem layers of CdSeS QDs of varying band gap within the photoactive anode of a QD solar cell (QDSC). An increase in power conversion efficiency of 1.97–2.81% with decreasing band gap was observed for single-layer CdSeS, thus indicating varying degrees of photon harvesting. In two- and three-layered tandem QDSCs, we observed maximum power conversion efficiencies of 3.2 and 3.0%, respectively. These efficiencies are greater than the values obtained for the three individually layered photoanodes. The synergy of using tandem layers of the ternary semiconductor CdSeS in QDSCs was systematically evaluated using transient spectroscopy and photoelectrochemistry.



INTRODUCTION

Low-band-gap metal chalcogenides such as CdS, CdSe, PbS, PbSe, and Sb₂S₃ are widely used as sensitizers in quantum dot solar cells (QDSCs).^{1–10} The simplicity of benchtop synthetic approaches makes QDSCs an excellent candidate for developing a transformative photovoltaic technology.¹¹ In both solid-state and liquid-junction QDSCs, a mesoporous oxide layer facilitates the charge separation by accepting electrons from the excited semiconductor. In a liquid-junction QDSC, the mesoporous nature of the TiO₂ working electrode not only increases the surface area for the deposition of semiconductor quantum dots (QDs) but also provides the necessary porosity for redox species to penetrate and scavenge the photogenerated holes.¹²

Successive ionic layer adsorption and reaction (SILAR)^{13–18} and chemical bath deposition (CBD)^{19–23} are commonly used methods for growing semiconductor QDs directly onto mesoscopic oxide (e.g., TiO₂) films. This in situ growth process is convenient for achieving a very high loading of QDs within the thin oxide film. However, QD films obtained by these methods lack control of the particle size and crystallinity. Further annealing at high temperature is necessary to render crystallinity. Alternatively, one can deposit presynthesized QDs onto a TiO₂ surface by direct deposition,^{24,25} linker-assisted attachment,^{26–28} or electrophoretic deposition (EPD).^{29–31} Since these QDs are synthesized at a relatively high temperature (~300 °C), they remain crystalline and thus exhibit sensitizing properties that are different than those prepared by SILAR or CBD.

In our earlier work, we reported the factors controlling charge injection into TiO₂ and charge recombination processes in CdSe/TiO₂ systems.^{32,33} Doping of CdS with Mn²⁺ during SILAR deposition improved the power conversion efficiency to values as high as 5.4%.¹⁸ Modification of CdS with such dopants allows the creation of long-lived excited states because of the spin-forbidden Mn d–d transition (⁴T₁–⁶A₁).³⁴ Another class of interesting semiconductor QDs are ternary metal chalcogenides, whose properties can be tuned by controlling the chalcogenide composition.^{35–37} The gradient alloy structure of CdSeS, for example, offers greater tunability of the absorption and emission bands throughout the visible region without changing the particle size.³⁷ To date, very little effort has been made to explore the alloy structure of ternary metal chalcogenides to tune the photon harvesting in QDSCs.³⁶

In the present work, we synthesized highly luminescent CdSeS QDs with a gradient alloy structure to obtain tandem semiconductor layers in QDSCs and synergistically harvest incident photons. The ease of sequential deposition of composition-selective ternary chalcogenides within the mesoscopic TiO₂ film enabled us to construct tandem layers of sensitizers and maximize the harvesting of incident visible photons within the QDSCs. The tunability of the absorption features allowed us to test the previously proposed concept of a rainbow solar cell.³⁸ The influence of the Se:S ratio in tuning

Received: October 31, 2012

Published: December 18, 2012

the excited-state properties of CdSeS QDs and its influence on the photovoltaic performance are discussed.

EXPERIMENTAL SECTION

Materials. Cadmium oxide (Alfa Aesar, 99.998%), oleic acid (Aldrich, 90%), 1-octadecene (Aldrich, 90%), selenium powder (Aldrich, 99.99%), sulfur powder (Alfa Aesar, 99%), trioctylphosphine (TOP) (Aldrich, 99%), methanol (Fisher Scientific, Certified ACS grade), toluene (Fisher Scientific, HPLC grade), and *n*-butanol (Fisher Scientific, Certified ACS grade) were used without further purification.

Synthesis of Quantum Dots. CdSeS QDs were synthesized using a previously reported method.³⁷ In a typical synthesis, 0.386 mmol of CdO was added to 1.63 mmol of oleic acid and 10 mL of 1-octadecene, and the solution was degassed for ~1 h at 80 °C. The reaction mixture was heated to 300 °C, where the solution became clear. Separately, Se and S powders in the desired ratio were dissolved in TOP under a nitrogen atmosphere. The premixed solution of Se and S was then injected into the reaction mixture at 300 °C. After this temperature was maintained for 30 s, the reaction mixture was allowed to cool to room temperature. *n*-Butanol was added to the reaction mixture to precipitate the QDs. The precipitated QDs were washed thoroughly five times using toluene and methanol to disperse and reprecipitate them in each cycle.

Characterization and Optical Measurements. Transmission electron microscopy (TEM) images were collected using a TITAN 80-300 electron microscope at an accelerating voltage of 300 kV. Scanning electron microscopy (SEM) images were collected using a Magellan 400 field-emission microscope with an operating voltage of 5 kV. UV-vis absorption spectra were recorded using a Varian Cary 50 Bio spectrophotometer. Photoluminescence spectra were recorded using a Horiba Fluorolog spectrophotometer. A 420 nm filter was introduced to exclude scattering from the excitation source. A solution of rhodamine 6G in ethanol (quantum efficiency = 96%) was used as a reference to determine the quantum efficiency (QE) of the QDs. Transient absorption spectroscopy measurements were performed using a Clark-MXR-2010 laser system (775 nm fundamental, 1 mJ/pulse, fwhm = 130 fs, 1 kHz repetition rate) combined with a Helios transient absorption detection system from Ultrafast Systems. The fundamental output beam was split 95/5; the 95% portion was frequency-doubled to 387 nm to become the pump beam, and the remaining 5% was used to generate a white-light continuum. Time-resolved transient absorption spectra were recorded using a spectrophotometric cell with provision for degassing the QDs deposited either on SiO₂ or TiO₂ films. The deposition of QDs on SiO₂ and TiO₂ films were carried out using a direct deposition method described previously.²⁸ The oxide films deposited on glass slides were immersed in the QD suspension in toluene overnight to achieve submonolayer coverage.

Nanocrystalline TiO₂ Electrode Preparation. Fluorine-doped tin oxide (FTO) glasses (Pilkington Glass, TEC 7, 2 mm thickness) were cleaned by sonication in detergent solution for 30 min followed by sonication in ethanol for 10 min. Three separate layers of TiO₂ films were deposited on FTO glass. First, a compact TiO₂ layer was deposited on the FTO glass by treating the glass in 40 mM TiCl₄ solution at 70 °C for 30 min and then washing with water and ethanol. A TiO₂ paste form (Solaronix, Ti-Nanoxide T/SP, particle size ~20 nm) was then deposited as the active layer by the doctor blade technique. The film was dried at room temperature and then kept at 80 °C for 1 h. The TiO₂ electrodes were annealed further at 500 °C in air for 1 h. A scattering layer of TiO₂ (CCIC, PST-400C, particle size ~400 nm) was finally deposited on top of the active layer by the doctor blade method. The electrodes were further dried and annealed at 500 °C for 1 h.

Electrophoretic Deposition of QDs. The FTO electrodes with and without deposited TiO₂ films were inserted in a quartz cuvette and kept at distance of 0.4 cm. QDs dispersed in toluene (2.5 mL) were added to the cuvette. A DC voltage of 60 V was applied for a particular time to allow the deposition of QDs from solution onto the TiO₂ electrode, which was connected to the positive terminal of the power

supply. To deposit multiple layers of QDs, the above step was repeated by replacing the solution with the QD suspension of the desired composition.

Solar Cell Fabrication. TiO₂ films with deposited QDs were used as photoanodes. The counter electrode was prepared from a composite of Cu₂S and reduced graphene oxide (RGO)³⁹ on cleaned FTO glass by doctor blading. The working and counter electrodes were assembled in a sandwich fashion using Parafilm as a spacer. A typical working electrode had an area of 0.20–0.25 cm². The electrolyte was prepared by dissolving 2 M Na₂S and 2 M S in water (*no methanol was used in the electrolyte*).

RESULTS AND DISCUSSION

Photophysical Properties. A series of CdSeS QDs with different Se:S ratios were synthesized. As discussed previously,³⁷ careful control of the Se:S ratio enables the band gap of CdSeS to be tuned from 2.57 to 2.05 eV. The optical properties and the band gaps obtained from the corresponding excitonic peaks of CdSeS with different Se:S ratios are summarized in Table 1. The change in the absorption maximum from ~480 to

Table 1. Absorption and Emission Characteristics of CdSeS QDs at Different Se:S Ratios

sample	abs peak (nm)	em peak (nm)	QE (%)	k_{ET} (s ⁻¹) ^a
CdS	476	483	27.4	—
Se:S = 1:75	524	546	59.9	—
Se:S = 1:50	539	558	62.0	5.5×10^{10}
Se:S = 1:25	565	581	42.4	2.2×10^{10}
Se:S = 1:5	593	608	14.7	1.5×10^9
CdSe	603	605	2.3	0.5×10^9 ^b

^aRate constant for electron transfer between excited CdSeS and TiO₂, as determined from transient absorption spectroscopy. ^bFor 4.2 nm CdSe QDs (data taken from ref 44).

~650 nm confirmed the decrease in the band gap with increasing Se content (Figure 1A). Relative emission spectra recorded using an excitation wavelength of 400 nm are shown in Figure 1B. The emission peaks are narrow and closely aligned with the edge of corresponding absorption spectrum, thus confirming the band-edge emission of these QDs. The prominent excitonic peak of these QDs with a bathochromic shift in the emission band confirmed that a narrow size distribution was successfully achieved in these samples. The QEs of these CdSeS QDs varied from 2.3 to 62.0%. As shown in the Figure 1B inset, the emission intensity increased with increasing S fraction, with a maximum QE of 62% at a Se:S ratio of 1:50. Such a high QE for CdSeS emission is similar to earlier reports where QEs of up to ~80% were observed.³⁷ The visual display of emission colors of the different CdSeS QDs dispersed in toluene under UV excitation is captured in Figure 1C.

This high photoluminescence efficiency arises from the naturally formed CdSe–CdS gradient from core to surface. As shown previously, the internal structure of such a CdSeS ternary compound allows the composition to vary gradually from CdSe in the core to CdS at the surface.⁴⁰ Such an internal structure is facilitated because of the higher reactivity of Cd toward Se than toward S. Recent quantum-mechanical calculations showed that the gradient structure also decreases the surface-related nonradiative decay, which in turn is reflected as a greater photoluminescence yield.⁴⁰

The size quantization effect in CdS and CdSe QDs has been well-established through the dependence of the band gap on

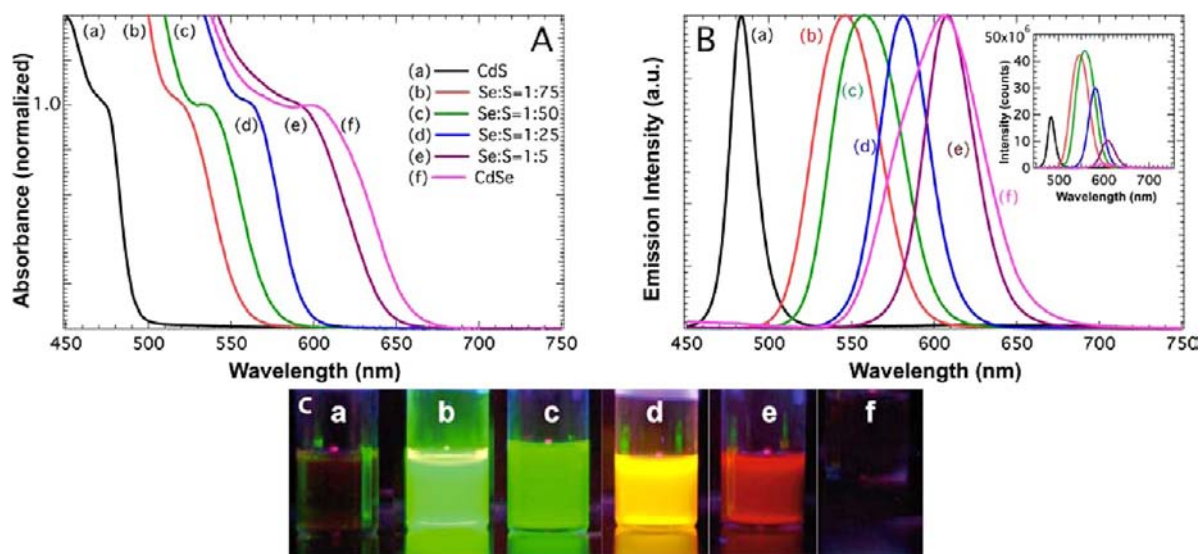


Figure 1. (A) Absorption spectra, (B) emission spectra, and (C) photographs under UV light of CdSe QDs with different Se:S ratios: (a) CdS; (b) Se:S = 1:75; (c) Se:S = 1:50; (d) Se:S = 1:25; (e) Se:S = 1:5; (f) CdSe. The absorption spectra were normalized to 1 at the excitonic peak. The emission spectra were recorded at an excitation wavelength of 400 nm and normalized to the emission peak. The inset of (B) shows the relative emission intensity variation for the different CdSe QDs.

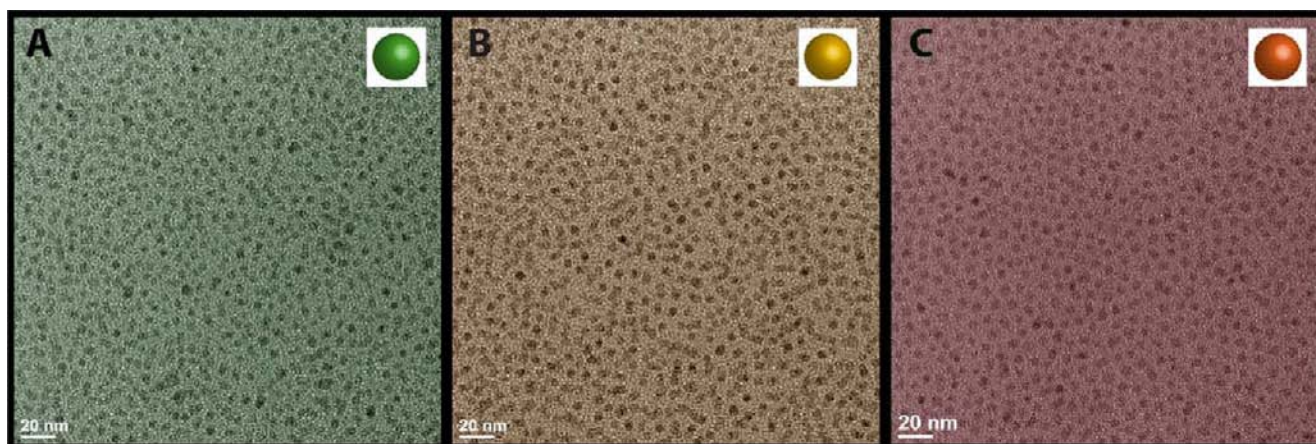


Figure 2. TEM images of CdSe QDs exhibiting (A) green (Se:S = 1:50), (B) orange (Se:S = 1:25), and (C) red (Se:S = 1:5) emission. The scale bar is 20 nm in each image.

the size of the particle. It was therefore interesting to determine whether the observed shifts in the absorption and emission spectra of different CdSe QDs (Figure 1) arise from changes in the composition or changes in the particle size. Figure 2 shows TEM images of CdSe QDs exhibiting (A) green (Se:S = 1:50), (B) orange (Se:S = 1:25), and (C) red (Se:S = 1:5) emission. The average diameters obtained from analysis of the TEM images were 4.5, 4.4, and 4.6 nm for green-, orange-, and red-emitting QD samples, respectively. These results confirmed that the size variation in these particles was minimal. Hence, the large shifts in the absorption and emission spectra observed for CdSe QDs with different Se:S ratios cannot be attributed to the variation in the particle size. The composition of Se and S in CdSe QDs dictates the effective band gap of CdSeS for a specific size of QD. Tuning the composition between Se and S in CdSeS provides the control of the effective band gap of the ternary chalcogenide.

Electron Transfer Dynamics. To assess the ability of CdSe QDs to be used in solar cells, we probed the excited-state dynamics and charge transfer processes on the oxide

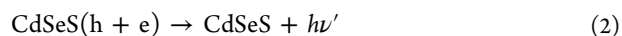
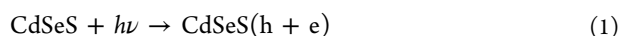
surface. The approach followed an earlier effort that used CdS and CdSe QDs deposited on mesoscopic TiO₂ films as a photoactive anodes. When employed in liquid-junction and solid-state solar cells, such photoanodes exhibit power conversion efficiencies in the range of 5–6%.^{41–43} Time-resolved transient absorption and emission spectroscopy techniques are convenient for probing the primary process of injecting electrons from excited QDs into oxide particles (TiO₂, ZnO, and SnO₂).⁴⁴

Three CdSe QDs prepared with Se:S ratios of 1:50 (green), 1:25 (orange), and Se:S = 1:5 (red) were chosen to probe the electron transfer from excited QDs into TiO₂ colloids using transient absorption spectroscopy. (On the basis of the color of emission, we refer to these colloids as green, orange, and red, respectively.) Transparent films of SiO₂ and TiO₂ on glass slides were first prepared by applying colloidal paste and then annealing at 500 °C. These films were then immersed separately in CdSeS suspensions to allow the adsorption of green-, orange-, and red-emitting CdSeS onto the TiO₂ surface. The direct adsorption method enables direct interactions

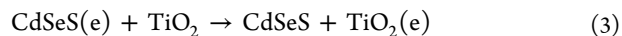
between CdSeS and TiO₂, as the coverage remains less than a monolayer with minimal aggregation effects.^{28,44}

Transient absorption spectra recorded using 387 nm laser pulse excitation of the red CdSeS QDs attached to TiO₂ and SiO₂ mesoscopic films are shown in Figure SI-1 in the Supporting Information. The disappearance of the characteristic 1S_{3/2}–1S_e transition of the CdSeS QDs is seen from the transient bleaching in the difference absorption spectra. The transient absorption spectra recorded immediately after the laser pulse excitation of CdSeS QDs attached to TiO₂ and SiO₂ exhibit similar spectral features. Hence, we can infer that the electronic transitions remain unperturbed by the nature of the oxide substrate. However, differences emerge in the rate at which the bleaching recovers. The absorption–time profiles of bleaching recovery for green, orange, and red QDs attached to SiO₂ and TiO₂ substrates are compared in Figure 3A–C, respectively.

Laser pulse excitation of CdSeS QDs adsorbed on SiO₂ and TiO₂ results in electron (e)–hole (h) separation (reaction 1) followed by recombination of the charge carriers (reaction 2):



On the TiO₂ surface, there is an additional deactivation pathway for the bleaching recovery in which the photo-generated electrons are injected into the TiO₂ nanoparticles (reaction 3):



As can be seen from Figure 3, the CdSeS bleaching recovery occurs faster on the TiO₂ surface than on the SiO₂ surface. This faster recovery confirms the contribution of reaction 3 to the overall disappearance of charge carriers. As discussed in earlier studies,^{28,32,33,44} the bleaching recovery occurs with a range of heterogeneous kinetics but can be fitted to a biexponential function. In case of QDs attached to SiO₂, the contribution due to electron injection from the QDs is negligible because this process is not energetically feasible. If we assume that the faster bleaching recovery seen on the TiO₂ surface is entirely due to the electron injection process, we can obtain the electron transfer rate constant (k_{ET}) from eq 4.

$$k_{\text{ET}} = \frac{1}{\tau(\text{TiO}_2)} - \frac{1}{\tau(\text{SiO}_2)} \quad (4)$$

where $\tau(\text{TiO}_2)$ and $\tau(\text{SiO}_2)$ are the lifetimes of the fast component of the bleaching recovery of the CdSeS/TiO₂ and CdSeS/SiO₂ films.

The electron transfer rate constants determined from the bleaching recovery traces in Figure 3 are summarized in Table 1. We considered the fast component of the recovery for estimating k_{ET} from eq 4 as it provides the upper limit for the observed electron transfer rate constant. The green QDs, which have the largest band gap, exhibit a k_{ET} value of $5.5 \times 10^{10} \text{ s}^{-1}$, which is nearly 2 orders of magnitude greater than the one observed for the red QDs. The different conduction band energies of these QDs provide different magnitudes of the driving force for injection of electrons into the TiO₂ nanoparticles (Scheme 1). Since decreasing the Se component

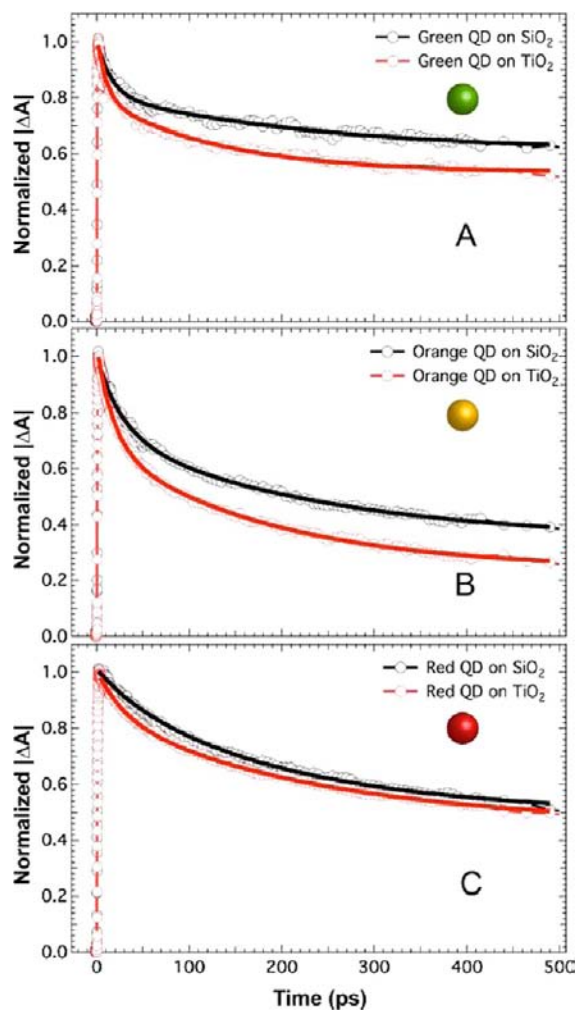
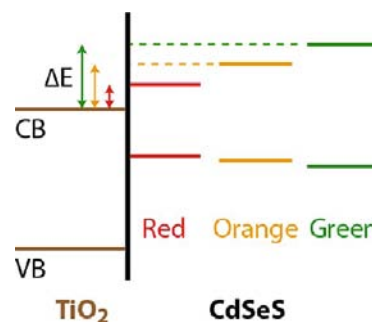


Figure 3. Kinetic traces of the excitonic decay of (A) green, (B) orange, and (C) red CdSeS QDs. The black and red traces correspond to QDs on TiO₂ and SiO₂, respectively. The solid lines represent corresponding biexponential kinetic fits. Decays are monitored at 539, 565 and 593 nm for green, orange and red QDs, respectively.

Scheme 1. Schematic Illustration of the Conduction and Valence Band Positions of the Green, Orange, and Red CdSeS QDs Relative to TiO₂



in CdSeS increases the band gap, we expect a concurrent shift in the conduction band to more negative potentials. For example, the difference between the conduction band energies of the green CdSeS QDs and TiO₂ is larger than those for the orange and red QDs, which in turn reflects a higher value of k_{ET} . A similar dependence of the electron transfer rate on the conduction band energy of quantized CdSe nanoparticles was established by varying the particle size.³² The Marcus many-

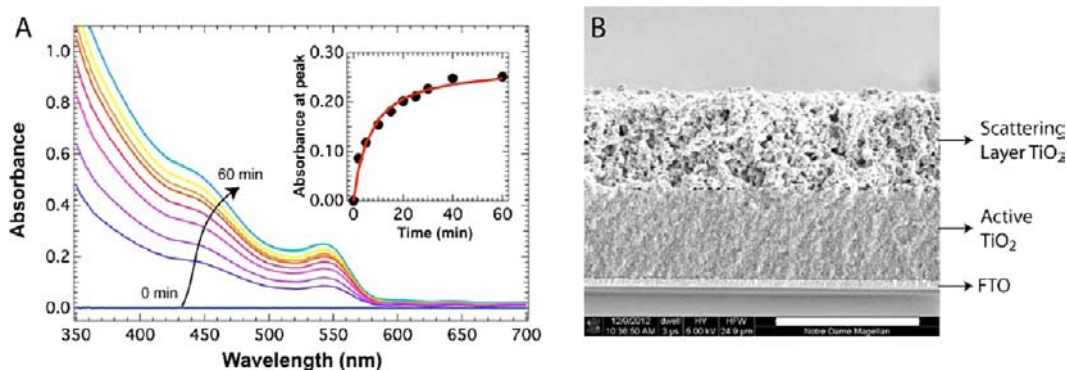


Figure 4. (A) Absorption spectra of red QDs attached to a transparent TiO₂ layer by EPD with a bias voltage of 60 V for deposition times of 0, 2, 5, 10, 15, 20, 25, 30, 40, and 60 min. The inset shows the variation of the absorption peak intensity at 550 nm with time. (B) Cross-sectional SEM image of the TiO₂ photoanode deposited with QDs by EPD. The scale bar represents a length of 10 μm.

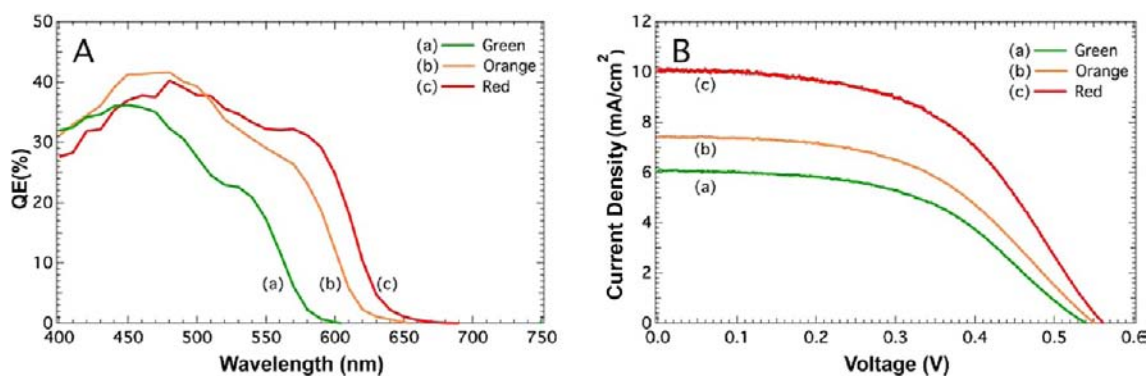


Figure 5. (A) IPCE spectra and (B) J - V characteristics of QDSCs with working electrodes containing (a) green, (b) orange, and (c) red CdSeS QDs. The working electrode areas were 0.24, 0.23, and 0.25 cm², respectively. A Cu₂S/RGO composite counter electrode was used, and aqueous 2 M Na₂S/2 M S served as the electrolyte. The performance of the solar cells was measured under AM 1.5 radiation with an incident power of 100 mW/cm².

state model was used to demonstrate the dependence of k_{ET} on the free energy difference, ΔG .^{33,44}

Electrophoretic Deposition and Absorption of QDs.

Various techniques have been employed to deposit metal chalcogenide QDs on TiO₂ and other oxide films. Although bifunctional linker molecule-assisted techniques are convenient for depositing chalcogenide QDs on TiO₂ surfaces, ligand exchange at the QD surface can often influence the excited-state dynamics. For example, during the ligand exchange of dodecylamine with mercaptopropionic acid (MPA) in CdSe QDs, one could readily observe creation of additional sulfur vacancies.⁴⁵ EPD is another useful technique in which the negatively charged QDs from solution are driven into the mesoscopic TiO₂ film under the influence of an applied electric field. The robust coverage achieved through EPD has been successfully employed in QDSCs.^{31,46} Of particular interest is the ease with which one can deposit sequential layers of QDs with different absorption properties and tailor the light-harvesting properties of the QDSC.

Figure 4A shows the absorption spectra of red QDs electrophoretically deposited onto a TiO₂ film during the application of a DC electric field. The absorption spectra of the electrode were recorded after application of a DC voltage of 60 V at fixed time intervals. The increase in absorbance of the electrode with EPD time confirmed the increased deposition of CdSeS QDs from solution onto the TiO₂ film. The absorption features of the electrophoretically deposited CdSeS film in Figure 4A shows characteristic excitonic peaks of red CdSeS.

The absorption features of these films are similar to those in the solution spectra, thus confirming the retention of the original properties of the pristine QDs following EPD. The rate of deposition of QDs during the EPD process was also monitored by the change in absorbance of CdSeS at a given wavelength with time (see the Figure 4A inset). Figure 4B shows the cross-sectional SEM image of the photoanode recorded after the electrodeposition of orange QDs within the TiO₂ film. The image shows the layered structure, including the blocking layer, the TiO₂/QD layer, and the scattering layer. Because of the extremely small size of the QDs, we were not able to map them within the TiO₂ layer.

Photoelectrochemical Performance of CdSeS in QDSCs. While most of the QDSC studies have focused on CdSe and CdS QDs, very few studies involving the utilization of ternary chalcogenide QDs exist.³⁶ The ability of CdSeS to inject electrons into TiO₂ efficiently makes this system an interesting candidate for the operation of QDSCs. Furthermore, the absorption tunability offers an opportunity to layer the individually separated green, orange, and red CdSeS QDs within the mesoscopic TiO₂ film and explore the construction of a rainbow solar cell.

Electrodes prepared by the EPD technique using highly emissive green-, orange-, and red-emitting CdSeS QDs were used as photoanodes in QDSCs. The concentration of QDs employed in the EPD solution was kept constant to maintain a similar absorbance (see the absorption spectra of EPD solutions in Figure SI-3). The total EPD duration for all samples was

Table 2. Photoelectrochemical Parameters of QDSCs Employing CdSeS/TiO₂ Films as Photoanodes

Configuration ^a	Sample-EPD time in min	J _{SC} (mA/cm ²)	V _{OC} (V)	FF	η (%)	Expected η (%)	Increase (%)
	Green-30	6.1	0.541	0.50	1.65	-	-
	Orange-30	7.5	0.549	0.51	2.10	-	-
	Red-30	10.2	0.566	0.51	2.94	-	-
	Green-15/Red-15	8.9	0.547	0.51	2.49	1.91	30.4
	Orange-15/Red-15	11.2	0.557	0.51	3.20	2.27	40.9
	Green-10/Orange-10/Red-10	10.9	0.548	0.50	3.00	1.87	60.4
	[Green+Orange+Red] mixed-30	8.5	0.552	0.50	2.34	2.21	5.9
	Red-15/Green-15	9.5	0.548	0.49	2.54	2.68	-5.2
	Red-15/Orange-15	10.7	0.567	0.49	2.92	2.77	5.4
	Red-10/Orange-10/Green-10	10.6	0.544	0.46	2.66	2.64	0.8

^aSequence of CdSeS (red, orange, and green) layers deposited on FTO. The illumination was from the FTO side. Other experimental conditions were same as in Figure 7B.

maintained at 30 min to ensure a constant amount of QD deposition. Absorption spectra were recorded after the EPD cycle to ensure similar loading levels of QDs. The QD-loaded photoanodes were treated with two cycles of ZnS by the SILAR method at room temperature. The overcoat of ZnS acted as a blocking layer to suppress the charge recombination process at the semiconductor–electrolyte interface.³¹ These electrodes were dried after washing with methanol and stored in the dark under N₂ atmosphere.

Figure 5A shows photoaction spectra of three CdSeS electrodes prepared using green, orange, and red QDs. The external quantum efficiency [or incident photocurrent to charge carrier generation efficiency (IPCE)] was determined by monitoring the photocurrent of the QDSCs at different monochromatic excitations. The onset of the photoresponse matches well with the absorption of the corresponding QDs reported in Figure SI-3. The peaks corresponding to the excitonic transitions are also seen in the IPCE spectra. The maximum IPCEs observed for these three electrodes were in the range of 35–42%.

The current density–voltage (*J*–*V*) characteristics of the green, orange, and red CdSeS QDs deposited within the pores of TiO₂ films are shown in Figure 5B. The short-circuit current density (*J*_{SC}), open-circuit potential (*V*_{OC}), fill factor (FF), and

overall power conversion efficiency (*η*) of QDSCs employing these three electrodes are summarized in Table 2. The *V*_{OC} values for the three electrodes were similar (0.541–0.566 V). However, the observed *J*_{SC} varied from 6.1 to 10.2 mA/cm² as the band gap of CdSeS decreased. Since the absorption of small-band-gap (red) CdSeS extends up to 640 nm, it is able to harvest a greater number of photons from the incident visible light and thus deliver a higher photocurrent. This trend is also reflected in the overall power conversion efficiencies of the QDSCs, which varied from 1.65% for the TiO₂ electrode sensitized with green CdSeS QDs to 2.94% for the electrode with red CdSeS QDs. The fill factors for all of these QDSCs were similar (~0.5), implying that these cells operated under similar electrochemical constraints as the incident light was converted into electricity. It should be noted that the Cu₂S/RGO composite counter electrode employed in the present study overcomes many of the limitations of Pt and brass counter electrodes in a sulfide/polysulfide electrolyte.³⁹

Photoelectrochemical Performance of Tandem Layers of CdSeS. Whereas the majority of QDSC studies have focused on utilizing a single type of QDs, a few attempts have been made to employ two different QDs to increase the absorption in the visible region. For example, sequential or codeposition of CdSe and CdS QDs on TiO₂ films has been

shown to improve the photoelectrochemical performance.^{39,47–49} In many of these QDSCs, the energy gained during ultra-band-gap excitation (viz., wavelengths shorter than the absorption onset) are simply lost in the thermalization process. Although proposals have been made to harvest hot electrons^{50,51} or multiple electron generation,⁵² the net gain in η has remained negligible. There are two other possibilities to engineer the light-harvesting features over a broader region and utilize the photons quite effectively: (i) coupling of dye molecules and semiconductor QDs to induce sensitization in a synergistic way and (ii) developing a tandem structure of semiconductor QDs in which the absorption of photons within the film is carried out in a systematic and gradient fashion. Several attempts have been made recently to design dye–QD composite systems. For example, suitable linking of a near-IR-absorbing squaraine dye with CdS or CdSe allowed the photocurrent response to be extended by sequential electron transfer⁵³ or Förster resonance energy transfer (FRET).⁵⁴ However, efforts to utilize sequentially deposited QD layers to engineer efficient light harvesting remains a challenge.

We will now discuss the design of multilayer QDSCs (with two or three tandem layers) by sequential deposition of green, orange, and red CdSeS QDs and explore the synergy of their tandem activity. Various combinations of deposition sequences were employed to optimize the photoelectrochemical performance of tandem-layered CdSeS photoanodes. The cell configuration and order of illumination of each layer are depicted in the first column of Table 2. For the construction of two-layer QDSCs, the TiO₂ electrode was first subjected to EPD for 15 min at 60 V with one CdSeS QD suspension. This step was followed by another EPD cycle with a different QD suspension. For example, in the case of the green/red bilayer film, the TiO₂ film was first subjected to EPD using the green QD suspension. This step was followed by the EPD using the red QD suspension. For three-layer QDSCs, green, orange, and red QD suspensions were used in three successive 10 min EPD cycles. The schematic diagram depicting the possible arrangement of green, orange, and red layers following the EPD is shown in Figure 6A. When excited with visible light from the FTO side, the green QDs are excited first, and the filtered light is absorbed by the orange QDs followed by the red QDs. It should be noted that during the first EPD cycle, the chosen

QDs are driven to the interior of the film, while the second (and third) cycles allow deposition of QDs away from the FTO surface. The loading of first-layer QDs close to the FTO surface is visualized from the coloration of the electrode through the transparent glass. For comparative studies, deposition of a mixture of QDs (Figure 6B) was also performed in a similar fashion by first mixing the three QD suspensions and then subjecting the mixture to a 30 min EPD cycle.

The IPCE spectra of QDSCs employing two or three different types of CdSeS QDs are shown in Figure 7A. (The absorption spectra of the working electrodes consisting of individual and two-layered QD/TiO₂ films are shown in Figure SI-4. The magnitudes of the absorption for the individual QD films and the composite films were estimated from the absorption vs EPD duration of CdSeS QDs in these electrodes.) The appearance of the photocurrent onset around 640 nm confirmed the participation of red QDs in all of these experiments. However, the magnitude of the maximum IPCE varied depending upon the layer configuration. The electrodes prepared with sequential deposition of orange/red (spectrum b) and green/orange/red (spectrum c) showed the best performance.

Figure 7B shows the J – V characteristics for different composite cells. The photovoltaic parameters of QDSCs recorded with various combinations of deposited CdSeS layers are summarized in Table 2. In all cases, V_{OC} exhibited little variation, with values ranging from 0.547 to 0.567 V. The J_{SC} values varied from 8.5 to 11.2 mA/cm². The best-performing composite QDSC (trace b in Figure 7B) had an electrode prepared with sequential layers of orange QDs followed by red QDs ($J_{SC} = 11.2$ mA/cm², $V_{OC} = 0.557$ V, and FF = 0.51). The net power conversion efficiency determined for the QDSC using the orange QD/red QD bilayer was 3.20%. Interestingly, the value of η for the QDSC employing this bilayer CdSeS electrode was higher than those for the QDSCs employing a single layer of orange (2.10%) or red (2.94%) QDs. The increase in η reflects the synergy of the two layers in capturing photons quite efficiently and thus enabling the delivery of a higher photocurrent. When a bilayer of QDs was deposited using green and red QDs, we observed an η value of 2.49%, which is greater than that for the QDSC employing green QDs alone but slightly lower than that using red QDs alone as the sensitizer. The three-layer QDSC with deposition of green QDs followed by orange QDs and red QDs exhibited a total power conversion efficiency of 3.00%, which is higher than the efficiency of photoanodes employing any of the QDs alone. These results highlight the importance of sequential arrangement of two different CdSeS QDs within the mesoscopic TiO₂ network to maximize the photon capture and participate in the charge injection process.

Synergy of Tandem QD Layers. We estimated the contribution of different CdSeS QDs in the bilayer electrode systems from the absorption spectra of the TiO₂/CdSeS films at different EPD times (Figure 4). For example, in an orange/red bilayer system, we expected ~80% orange QDs to be deposited in the first EPD cycle and the remaining 20% red QDs to be deposited in the second cycle. If the observed η value is a simple additive effect, we would expect η of the orange/red bilayer electrode to be the sum of 80% of the orange QDSC value and 20% of the red QDSC value. Similar η estimates based on the additive effect were made from the contributions of different CdSeS layers, and the values are compared in Table 2.

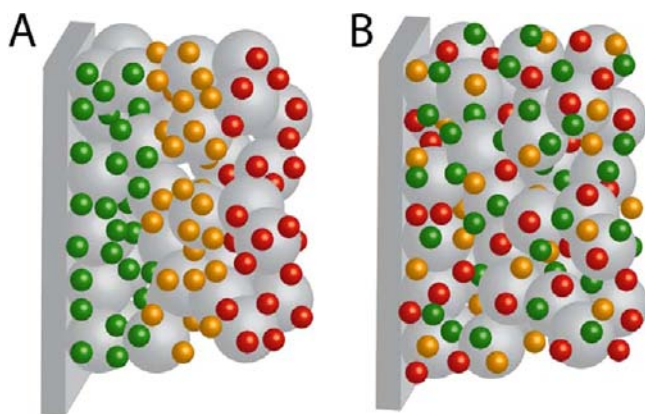


Figure 6. Schematic illustrations of QDSCs formed by sequential and simultaneous deposition of CdSeS QDs. (A) Sequentially deposited green, orange, and red QDs constituting the rainbow QDSC structure. (B) QDSC structure formed using premixed [green + orange + red] QDs.

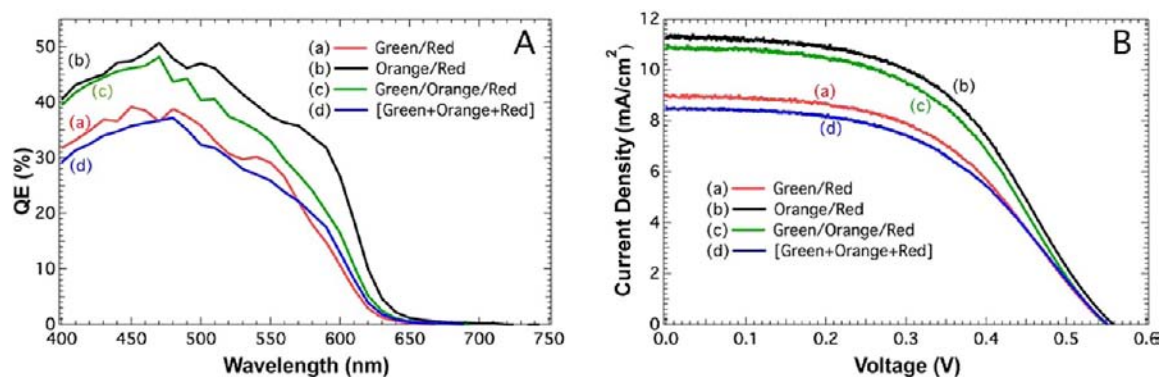
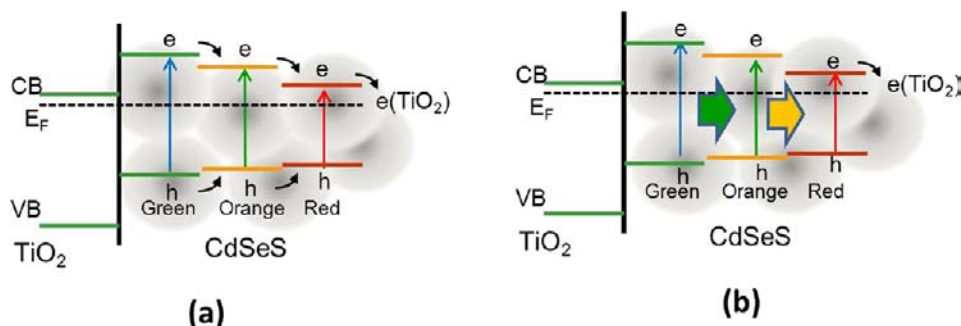


Figure 7. (A) IPCE spectra and (B) J - V characteristics of different composite working electrodes containing (a) green/red, (b) orange/red, or (c) green/orange/red sequential layers or (d) a layer of premixed [green + orange + red] CdSeS QDs deposited by EPD. The working electrode areas were 0.24, 0.21, 0.21, and 0.22 cm², respectively. A Cu₂S/RGO composite counter electrode was used, and aqueous 2 M Na₂S/2 M S served as the electrolyte. The performance of the solar cells was measured under AM 1.5 radiation with an incident power of 100 mW/cm².

Scheme 2. Illustration of (a) Electron Transfer and (b) Energy Transfer Processes between Green, Orange, and Red QDs Assembled in a Tandem Architecture (Electrons Are Injected from Red QDs into TiO₂)



The observed efficiency of 3.20% for the orange/red-layered QDSC is greater than the value of 2.27% obtained from the estimation of the additive effect. The nearly 41% increase in the efficiency of this orange/red bilayer QDSC shows that the tandem layers of CdSeS with different absorptive ranges are beneficial for improving the performance of the QDSC. Similarly, the green/red-layered QDSC shows an η increase of 30% compared with the expected 1.91%. To further establish the synergy of the tandem-layer configuration, we compared the performance of the QDSC containing the sequentially deposited three-layer CdSeS/TiO₂ electrode (trace c in Figure 7B) with that of the QDSC containing the premixed layer of three QDs (trace d in Figure 7B). The three-component composite QDSC was constituted with 70% green QDs, 20% orange QDs, and 10% red QDs. The net power conversion efficiency with sequentially layered QDs was 3.0%, which is greater than the η value with premixed QDs (2.34%). The increase in η of sequentially layered three component QDSC is 60% compared with the calculated efficiency of 1.87%. These results further support the argument that the systematic layering of QDs can provide synergy for capturing and converting a wide array of photons in the visible region.

Scheme 2 illustrates two possible scenarios for observing the synergy of layered QDs in tandem. In the first case, the alignment of band energies would allow an electron transfer cascade from larger-band-gap QDs to smaller-band-gap QDs, resulting in the accumulation of electrons in the latter. These electrons would then be injected into TiO₂ nanoparticles and transported across TiO₂ network. The other scenario would involve energy transfer from larger-band-gap QDs to smaller-

band-gap QDs, thus concentrating excitation in the red QDs. This would cause red QDs to be the major participant in the electron transfer process. The feasibility of such energy transfer between QDs with different band gaps has been demonstrated by Choi et al.⁵⁵ By employing time-resolved emission studies, these researchers were able to demonstrate the combined effect of energy and electron transfer processes in two different sizes of CdSe QDs deposited on TiO₂ films. The layered structure in their example was obtained by the Langmuir–Blodgett technique. Although it is difficult at this stage to pinpoint the contributions of the electron and energy transfer routes presented in Scheme 2, the synergistic effects observed with the tandem architecture highlight the possible role of both of these pathways in improving the performance of composite QDSCs.

CONCLUSIONS

Highly luminescent ternary chalcogenide QDs with gradient composition offer new ways to design QDSCs with selective absorption in the visible region. The electrophoretic deposition of crystalline CdSeS nanoparticles within the mesoscopic TiO₂ film forms layered structures within the mesoscopic TiO₂ film and thus maximizes the light-harvesting capability of QDSCs. The sequential layering of larger-band-gap CdSeS QDs followed by smaller-band-gap QDs provides a better synergy for harvesting incident photons across the visible spectrum. Power conversion efficiencies of 3.2 and 3.0% obtained for QDSCs with two and three layers of QDs, respectively, represent synergistic effects during the operation of tandem-layered QDSCs. This maiden concept of utilizing ternary metal

chalcogenides in the design of tandem-layered QDSCs paves the way to new strategies for improving the efficiency of solar cells.

■ ASSOCIATED CONTENT

● Supporting Information

Ultrafast transient absorption spectra at different times for the red CdSeS QDs, absorption spectra of the EPD solutions and the films, comparison of solar cell performance with and without ZnS treatment, and cross-sectional SEM image of a photoanode. This material is available free of charge via the Internet at <http://pubs.acs.org>.

■ AUTHOR INFORMATION

Corresponding Author

pkamat@nd.edu

Notes

The authors declare no competing financial interest.

■ ACKNOWLEDGMENTS

The research described herein was supported by the Division of Chemical Sciences, Geosciences, and Biosciences, Office of Basic Energy Sciences, Office of Science, United States Department of Energy through Grant DE-FC02-04ER15533. This is contribution number NDRL 4943 from the Notre Dame Radiation Laboratory. We thank James Radich, S. Krishnamurthy, and Douglas Hines for their assistance with SEM, TEM, and transient absorption spectroscopy measurements.

■ REFERENCES

- (1) Smotkin, E. S.; Cervera, M. S.; Bard, A. J.; Campion, A.; Fox, M. A.; Mallouk, T.; Webber, S. E.; White, J. M. *J. Phys. Chem.* **1987**, *91*, 6.
- (2) Frame, F. A.; Osterloh, F. E. *J. Phys. Chem. C* **2010**, *114*, 10628.
- (3) Liu, L.; Hensel, J.; Fitzmorris, R. C.; Li, Y.; Zhang, J. Z. *J. Phys. Chem. Lett.* **2010**, *1*, 155.
- (4) Amirav, L.; Alivisatos, A. P. *J. Phys. Chem. Lett.* **2010**, *1*, 1051.
- (5) Wang, Z.-T.; Du, Y.; Dohnálek, Z.; Lyubinsky, I. *J. Phys. Chem. Lett.* **2010**, *1*, 3524.
- (6) Kamat, P. V.; Tvrđy, K.; Baker, D. R.; Radich, J. G. *Chem. Rev.* **2010**, *110*, 6664.
- (7) Kamat, P. V. *J. Phys. Chem. C* **2008**, *112*, 18737.
- (8) Mora-Sero, I.; Bisquert, J. *J. Phys. Chem. Lett.* **2010**, *1*, 3046.
- (9) Kramer, I. J.; Sargent, E. H. *ACS Nano* **2011**, *5*, 8506.
- (10) Shalom, M.; Tachan, Z.; Bouhadana, Y.; Barad, H.-N.; Zaban, A. *J. Phys. Chem. Lett.* **2011**, *2*, 1998.
- (11) Genovese, M. P.; Lightcap, I. V.; Kamat, P. V. *ACS Nano* **2012**, *6*, 865.
- (12) Chakrapani, V.; Baker, D.; Kamat, P. V. *J. Am. Chem. Soc.* **2011**, *133*, 9607.
- (13) Kannianen, T.; Lindroos, S.; Ihanus, J.; Leskela, M. *J. Mater. Chem.* **1996**, *6*, 983.
- (14) Sankapal, B. R.; Mane, R. S.; Lokhande, C. D. *MRS Bull.* **2000**, *35*, 177.
- (15) Lee, H.; Leventis, H. C.; Moon, S. J.; Chen, P.; Ito, S.; Haque, S. A.; Torres, T.; Nuesch, F.; Geiger, T.; Zakeeruddin, S. M.; Grätzel, M.; Nazeeruddin, M. K. *Adv. Funct. Mater.* **2009**, *19*, 2735.
- (16) Lee, H. J.; Chen, P.; Moon, S.-J.; Sauvage, F.; Sivula, K.; Bessho, T.; Gamelin, D. R.; Comte, P.; Zakeeruddin, S. M.; Seok, S. I.; Grätzel, M.; Nazeeruddin, M. K. *Langmuir* **2009**, *25*, 7602.
- (17) Lee, H.; Wang, M. K.; Chen, P.; Gamelin, D. R.; Zakeeruddin, S. M.; Grätzel, M.; Nazeeruddin, M. K. *Nano Lett.* **2009**, *9*, 4221.
- (18) Santra, P. K.; Kamat, P. V. *J. Am. Chem. Soc.* **2012**, *134*, 2508.
- (19) Nikumbh, M.; Gore, V.; Gore, R. B. *Renewable Energy* **1997**, *11*, 459.
- (20) Mane, R. S.; Roh, S. J.; Joo, O. S.; Lokhande, C. D.; Han, S. H. *Electrochim. Acta* **2005**, *50*, 2453.
- (21) Hankare, P. P.; Chate, P. A.; Chavan, P. A.; Sathe, D. J. *J. Alloys Compd.* **2008**, *461*, 623.
- (22) Hossain, M. F.; Biswas, S.; Takahashi, T. *Thin Solid Films* **2009**, *518*, 1599.
- (23) Patil, S. B.; Singh, A. K. *Appl. Surf. Sci.* **2010**, *256*, 2884.
- (24) Gur, I.; Fromer, N. A.; Geier, M. L.; Alivisatos, A. P. *Science* **2005**, *310*, 462.
- (25) Shen, Y.; Bao, J.; Dai, N.; Wu, J.; Gu, F.; Tao, J. C.; Zhang, J. C. *Appl. Surf. Sci.* **2009**, *255*, 3908.
- (26) Mann, J. R.; Watson, D. F. *Langmuir* **2007**, *23*, 10924.
- (27) Watson, D. F. *J. Phys. Chem. Lett.* **2010**, *1*, 2299.
- (28) Pernik, D.; Tvrđy, K.; Radich, J. G.; Kamat, P. V. *J. Phys. Chem. C* **2011**, *115*, 13511.
- (29) Islam, M. A.; Xia, Y.; Telesca, D. A.; Steigerwald, M. L.; Herman, I. P. *Chem. Mater.* **2004**, *16*, 49.
- (30) Jia, S.; Banerjee, S.; Herman, I. P. *J. Phys. Chem. C* **2008**, *112*, 162.
- (31) Salant, A.; Shalom, M.; Tachan, Z.; Buhbut, S.; Zaban, A.; Banin, U. *Nano Lett.* **2012**, *12*, 2095.
- (32) Robel, I.; Subramanian, V.; Kuno, M.; Kamat, P. V. *J. Am. Chem. Soc.* **2006**, *128*, 2385.
- (33) Robel, I.; Kuno, M.; Kamat, P. V. *J. Am. Chem. Soc.* **2007**, *129*, 4136.
- (34) Bhargava, R. N.; Gallagher, D.; Hong, X.; Nurmikko, A. *Phys. Rev. Lett.* **1994**, *72*, 416.
- (35) Al-Salim, N.; Young, A. G.; Tilley, R. D.; McQuillan, A. J.; Xia, J. *Chem. Mater.* **2007**, *19*, 5185.
- (36) Ma, W.; Luther, J. M.; Zheng, H.; Wu, Y.; Alivisatos, A. P. *Nano Lett.* **2009**, *9*, 1699.
- (37) Jang, E.; Jun, S.; Pu, L. *Chem. Commun.* **2003**, 2964.
- (38) Kongkanand, A.; Tvrđy, K.; Takechi, K.; Kuno, M. K.; Kamat, P. V. *J. Am. Chem. Soc.* **2008**, *130*, 4007.
- (39) Radich, J. G.; Dwyer, R.; Kamat, P. V. *J. Phys. Chem. Lett.* **2011**, *2*, 2453.
- (40) Sarma, D. D.; Nag, A.; Santra, P. K.; Kumar, A.; Sapra, S.; Mahadevan, P. *J. Phys. Chem. Lett.* **2010**, *1*, 2149.
- (41) Pattantyus-Abraham, A. G.; Kramer, I. J.; Barkhouse, A. R.; Wang, X.; Konstantatos, G.; Debnath, R.; Levina, L.; Raabe, I.; Nazeeruddin, M. K.; Grätzel, M.; Sargent, E. H. *ACS Nano* **2010**, *4*, 3374.
- (42) Moon, S.-J.; Itzhaik, Y.; Yum, J.-H.; Zakeeruddin, S. M.; Hodes, G.; Grätzel, M. *J. Phys. Chem. Lett.* **2010**, *1*, 1524.
- (43) Gao, J.; Perkins, C. L.; Luther, J. M.; Hanna, M. C.; Chen, H.-Y.; Semonin, O. E.; Nozik, A. J.; Ellingson, R. J.; Beard, M. C. *Nano Lett.* **2011**, *11*, 3263.
- (44) Tvrđy, K.; Frantsov, P.; Kamat, P. V. *Proc. Natl. Acad. Sci. U.S.A.* **2011**, *108*, 29.
- (45) Baker, D. R.; Kamat, P. V. *Langmuir* **2010**, *26*, 11272.
- (46) Lightcap, I. V.; Kamat, P. V. *J. Am. Chem. Soc.* **2012**, *134*, 7109.
- (47) Deng, M. H.; Zhang, Q. X.; Huang, S. Q.; Li, D. M.; Luo, Y. H.; Shen, Q.; Toyoda, T.; Meng, Q. B. *Nanoscale Res. Lett.* **2010**, *5*, 986.
- (48) Tian, J.; Gao, R.; Zhang, Q.; Zhang, S.; Li, Y.; Lan, J.; Qu, X.; Cao, G. *J. Phys. Chem. C* **2012**, *116*, 18655.
- (49) Shalom, M.; Buhbut, S.; Tirosh, S.; Zaban, A. *J. Phys. Chem. Lett.* **2012**, *3*, 2436.
- (50) Pandey, A.; Guyot-Sionnest, P. *J. Phys. Chem. Lett.* **2010**, *1*, 45.
- (51) Tisdale, W. A.; Williams, K. J.; Timp, B. A.; Norris, D. J.; Aydil, E. S.; Zhu, X. Y. *Science* **2010**, *328*, 1543.
- (52) Beard, M. C. *J. Phys. Chem. Lett.* **2011**, *2*, 1282.
- (53) Choi, H.; Nicolaescu, R.; Paek, S.; Ko, J.; Kamat, P. V. *ACS Nano* **2011**, *5*, 9238.
- (54) Choi, H.; Santra, P. K.; Kamat, P. V. *ACS Nano* **2012**, *6*, 5718.
- (55) Choi, S.; Jin, H.; Bang, J.; Kim, S. *J. Phys. Chem. Lett.* **2012**, *3*, 3442.